5

Force Field Spectroscopy in Three Dimensions

André Schirmeisen, Hendrik Hölscher, and Udo D. Schwarz

Abstract. Atomic resolution images in noncontact atomic force microscopy (NC-AFM) reflect planes of constant frequency shift. To draw conclusions on the chemical activity at specific surface sites, however, the force acting between tip and sample should be known locally rather than the frequency shift. This is not an easy translation due to the nonlinear nature of the relationship between the two.

To overcome this problem, several groups have developed an extension to NC-AFM, dynamic force spectroscopy, which allows the precise, distance-dependent measurement of tip–sample forces. The forces are determined from frequency shift vs. distance curves by mathematical analysis. By combining many of these curves in a raster grid, the full three-dimensional surface force field can be probed with atomic resolution as it extends into vacuum. This chapter reviews experiments performed on NiO, NaCl, KBr, and graphite that illustrate the strengths and weaknesses of the different experimental approaches as well as the type of results that can be obtained.

5.1 Introduction

Since its invention in 1986 [1], the success of atomic force microscopy (AFM) roots in its combination of high resolution imaging capabilities and broad versatility, as it is capable of imaging almost any type of surface without the need for tedious sample preparation. Force microscopy relies on the detection of interaction forces between a raster-scanned sharp tip and the investigated surface, with the corresponding signal being recorded as a function of the tip's lateral position. Typically, finite tip–sample contact areas cause the net interaction to be averaged over the often dozens or even hundreds of atoms involved in the process of contrast formation, with individual atom–atom interactions not explicitly being exploited in conventional AFM imaging modes.

By employing atomically sharp tips in conjunction with the right experimental approach, it is nevertheless possible to measure signals that are dominated by interatomic forces caused by just the tip's foremost atom. To avoid the above-mentioned averaging effect due to the formation of tip–sample

S. Morita et al. (eds.), *Noncontact Atomic Force Microscopy*,
NanoScience and Technology,
DOI: 10.1007/978-3-642-01495-6_5, © Springer-Verlag Berlin Heidelberg 2009

contact areas comprising multiple atoms, "dynamic" modes, that is, modes where the tip is oscillated close to the surface, are usually being applied [2,3]. If the tip is scanned in a horizontal raster, the corresponding approach is called *dynamic force microscopy* (DFM) and enables atomic resolution imaging on many different material classes, including metals [4–6], semiconductors [3, 7–10], and insulators [11–14]. Alternatively, dynamic mode operation also allows the measurement of the distance-dependent tip–sample forces ("force distance curves") at specific lattice sites, which is then referred to as *dynamic force spectroscopy* (DFS) [15–19]. Recently, combination of the two abilities has culminated in the chemical identification of surface atoms [20]. Moreover, it has been demonstrated how a systematic acquisition of adjacent force distance curves allows to determine three-dimensional (3D) atomic force fields above the sample surface [21, 22].

The recent growing interest [23–28] in the force field technique stems from several aspects. From the technical perspective, the availability of 3D atomic-scale force field maps facilitates assessing lateral relaxations of the tip–sample contact occurring during the approach as well as experimental artifacts like piezoelectric drift. From the scientific viewpoint, characterization of the vertical force field allows to calculate the potential energy barriers [23] and landscapes [27].

Experimental access to the spatial variation of the potential energy with sublattice resolution is difficult. Conventional techniques [29] rely on the measurement of the dynamic behavior of test adsorbates by, for example, diffusion experiments and field emission techniques [30]. Direct observation of adatom motion with the field ion microscope [31] or the scanning tunneling microscope [32] is possible, but limited to conducting surfaces. Potential energy barriers can be extracted from those experiments (cf. Fig. 5.1a), but the full spatial characterization of the energy landscape remains a challenge. Ideally, one would measure the site-specific variation of the interaction energy between a test molecule and the substrate. A viable technical solution is the measurement of forces between a single atom-terminated sharp asperity and a flat surface, a basic geometry that is naturally instantiated by scanning probe microscopy techniques (Fig. 5.1b).

An added benefit of this approach is that it also recovers lateral atomic forces [22, 24], which has been exploited to determine the lateral force needed to move an atom on a surface [27]. A combination of the simultaneously measured lateral and vertical forces allows to obtain atomic scale force vector fields [33]. Finally, high-precision, low-drift measurements performed at low temperature could successfully probe the 3D force field of graphite with picometer resolution in x, y, and z and piconewton force resolution [34]. From this dense three-dimensional raster, force maps in all directions could be obtained at all locations within the covered space. This lead in particular to atomically resolved true force images in topview perspective rather than just to vertical xz maps.

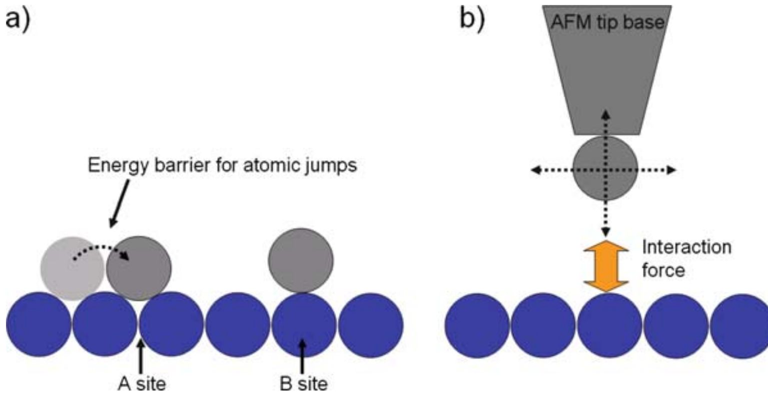

Fig. 5.1. Basic principle of potential energy landscape measurements. **(a)** Surface atoms are adsorbed at lattice sites where the potential energy exhibits a local minimum ("A sites"). During surface diffusion, lateral motion manifests as jumps over the barriers between adjacent energy minima ("B sites"). **(b)** By measuring the interaction forces between a single atom-terminated tip and the surface, the potential energy landscape can be recovered

5.2 Three-Dimensional Force Field Spectroscopy: The Technique

To achieve high resolution, most DFM experiments are performed in ultrahigh vacuum (UHV), where clean surfaces without unwanted adsorbates can be prepared. Because of the high quality factors Q that oscillating AFM cantilevers exhibit in vacuum, it is advantageous to apply the *frequency modulation* (FM) *scheme* introduced by Albrecht et al. [2] to excite the cantilever and detect its motion. In this scheme, the cantilever is "self-oscillated," that is, an electronic feedback system is used to drive the cantilever at its actual resonance frequency f. As f depends on the forces acting on the tip, the difference Δf between f and the eigenfrequency of the undisturbed cantilever f_0 is a measure for the strength of the tip–sample interaction and ultimately the tip–sample distance. This differs from amplitude modulation (AM) based imaging modes [36–38], where the cantilever is externally driven with a fixed driving frequency, which are best used in low-Q conditions such as in air or liquids. In this section, we discuss the experimental set-up of FM-AFM, explain the origin of the detected frequency shift Δf, and present methods that allow tip–sample forces to be recovered from distance-dependent Δf measurements.

5.2.1 Experimental Set-up

Figure 5.2 shows schematically the basic set-up of an atomic force microscope operated in frequency modulation mode. The movement of the cantilever with spring constant c_z is measured by detecting the position of a laser beam

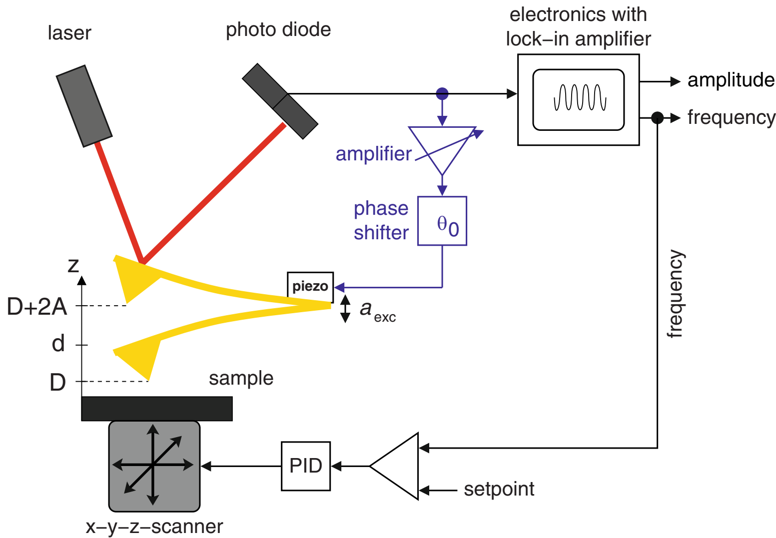

Fig. 5.2. A dynamic force microscope operated in frequency modulation mode, as it is often realized for UHV applications. The key feature is the positive feedback used to "self-oscillate" the cantilever. A laser beam is reflected at the backside of a cantilever that has an integrated sharp tip at its free end. Bending of the cantilever causes a deflection of the reflected beam, which is detected by a photo diode. The resulting signal is subsequently amplified and phase-shifted before it is used to drive the dither piezo exciting the cantilever. The measured quantity is the frequency shift $\Delta f = f - f_0$ caused by the tip–sample interaction, which serves as the feedback signal controlling the tip–sample distance

reflected from the cantilever backside on a photo diode. This signal is then fed into an amplifier featuring the possibility of *automatic gain control* (AGC) [2] and subsequently used to excite a piezo that drives the cantilever. The time delay between the excitation signal and cantilever deflection is adjusted to a phase shift of 90°, leading to an oscillation at resonance. The measured quantity is the *frequency shift* Δf representing the difference between the actual resonance frequency f and the eigenfrequency f_0 of the free cantilever, that is, $\Delta f = f - f_0$. Two different modes have been established: The *constant amplitude* mode [2], where the excitation amplitude a_{exc} of the dither piezo is regulated by the AGC electronics to maintain a constant value of the oscillation amplitude A, and the *constant excitation mode* [39], where a_{exc} is kept constant. In the following, we focus on the constant amplitude mode, which is the dominant mode of operation in most studies published to date.

For imaging, the frequency shift Δf is used to control the tip–sample distance D (distance of closest approach during an oscillation cycle, cf. Fig. 5.2). Thus, if the system's feedback loop regulates the frequency shift to remain on a constant setpoint value, the acquired data reflects planes of constant Δf.

Usually regarded as representing the "topography" of the surface, such planes of constant frequency shift are in reality hard to interpret in terms of physical quantities, as constant Δf does not equal constant force. Even worse, the determination of tip–sample interaction forces solely from DFM images is generally impossible. Therefore, we concentrate in this section on the earlier introduced *dynamic force spectroscopy* (DFS) approach, where the recording of the frequency shift Δf as a function of the tip–sample distance D ("frequency shift curves" or "$\Delta f(D)$ curves") is used to determine the tip–sample force with high resolution.

An example for such measurements is given in Fig 5.3a, where $\Delta f(D)$ curves acquired at different oscillation amplitudes are depicted. All curves

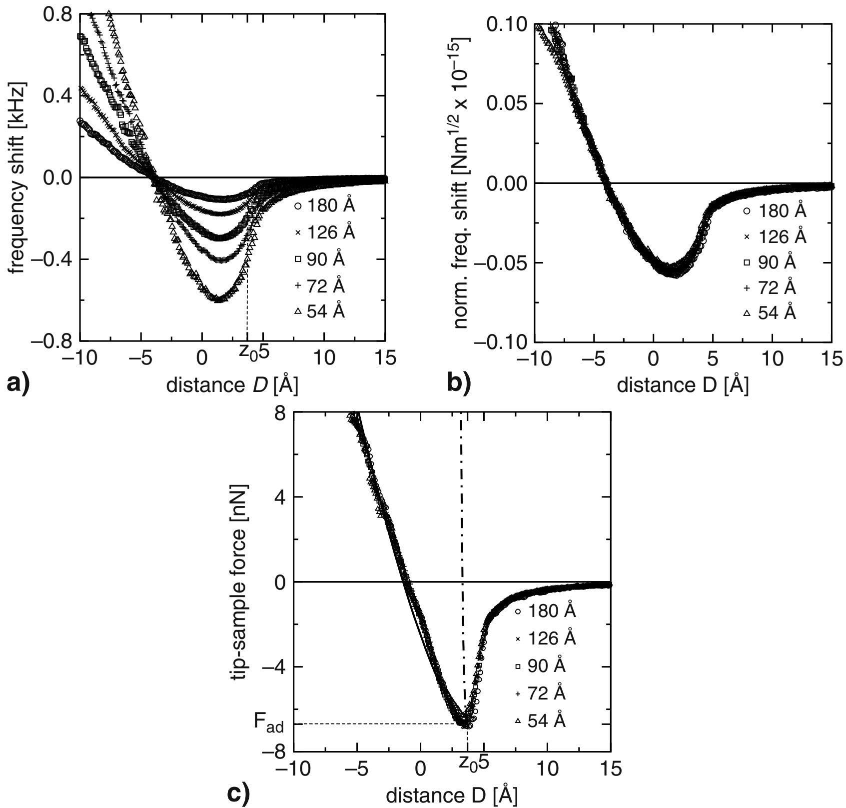

Fig. 5.3. **(a)** Experimental frequency shift vs. distance curves acquired with a silicon tip and a graphite sample for different oscillation amplitudes A (54–180 Å) in UHV at 80 K [40]. The curves are shifted along the D axis to make them comparable. **(b)** Application of (5.5) to the frequency shift curves shown in (**a**). The normalized frequency shift γ is almost identical for all amplitudes. **(c)** Example for the application of dynamic force spectroscopy. The *grey symbols* reflect the tip–sample force as calculated from the experimental data of panel (**a**) using (5.6)

exhibit a similar overall shape, but differ in magnitude depending on the oscillation amplitude A and tip–sample distance D. During the approach of the tip towards the sample surface, the frequency shift decreases and reaches a minimum. With a further reduction of the nearest tip–sample distance, the frequency shift increases again and becomes positive. In the next subsection, we will explain how these data can be used to recover the tip–sample forces.

5.2.2 The Interrelation Between Frequency Shift and Tip–Sample Forces

A quantitative formula for the frequency shift can be obtained by the application of different mathematical treatments based on the assumption that the tip oscillations are still nearly sinusoidal, that is, the tip position z as a function of the time t can be still described by $z(t) := A\cos(2\pi f t)$. Such an approach is justified if the tip–sample interaction force F_{ts} is much smaller than the retracting cantilever force and results in the equation

$$\Delta f = -\frac{f_0^2}{A c_z} \int_0^{1/f_0} F_{\mathrm{ts}}\left[z(t), \dot{z}(t)\right] \cos(2\pi f_0 t)\,\mathrm{d}t \tag{5.1}$$

$$= -\frac{f_0}{\pi A^2 c_z} \int_{-A}^{A} \frac{F_{\rightarrow} + F_{\leftarrow}}{2} \frac{z'}{\sqrt{A^2 - z'^2}}\,\mathrm{d}z', \tag{5.2}$$

where $F_{\rightarrow}$ and $F_{\leftarrow}$ describe the tip–sample force during approach and retraction, respectively. In most cases, these two forces are considered to be equal, that is, hysteresis-free behavior is assumed. Nonetheless, as the frequency shift is a measure of the complete oscillation cycle of the cantilever, it is determined by the averaged tip–sample force $F_{\mathrm{ts}} = (F_{\rightarrow} + F_{\leftarrow})/2$. For completeness, we also give the formula for the calculation of the energy ΔE that is dissipated per oscillation cycle:

$$\Delta E(A) = \pi c_z \left(A\, a_{\mathrm{exc}} - \frac{A^2}{Q} \right). \tag{5.3}$$

For a more detailed derivation of these formulas see, for example, [41–43].

The integral in (5.2) can be further simplified with the assumption that the decay length of the tip–sample interaction is much smaller than the oscillation amplitude. This so-called *large amplitude limit* was first analyzed by Giessibl [41] and is typically reached if the oscillation amplitudes are larger than 5 nm. Because of the assumed large amplitude, the weighting term in the integral (5.2) can be expanded at $z' = -A$ to $\approx -\sqrt{A/2(A + z')}$. By shifting the origin of the z-axis to $z = z' + D + A$ and extending the upper limit of the integral to infinity, the frequency shift can be simplified to [45]

$$\Delta f^{\mathrm{la}} = \frac{1}{\sqrt{2}\pi} \frac{f_0}{c_z A^{3/2}} \int_D^\infty \frac{F_{\mathrm{ts}}(z)}{\sqrt{z-D}}\,\mathrm{d}z. \quad (5.4)$$

The index "la" highlights the restriction of the formula to the large-amplitude limit.

It is interesting to note that the integral in this equation is independent of the amplitude, as it depends solely on the tip–sample force F_{ts} and the tip–sample distance D. The experimental parameters (c_z, f_0, and A) appear only as prefactors. Therefore, Giessibl [41] defined the *normalized frequency shift*

$$\gamma(z) = \frac{c_z A^{3/2}}{f_0} \Delta f(z), \quad (5.5)$$

which is a useful quantity if experiments obtained with different oscillation amplitudes and/or cantilevers ought to be compared. Additionally, it allows to elegantly link theoretical calculations with experiments. The validity of (5.5) is nicely demonstrated by its application to the frequency shift curves presented earlier in Fig. 5.3a. As shown in Fig. 5.3b, all curves obtained for different amplitudes collapse into one universal γ curve, which depends only on the actual tip–sample distance D. This scaling law is also useful to calibrate the oscillation amplitude [44].

For typical DFM set-ups, it is straightforward to measure the frequency shift with a fixed oscillation amplitude A as a function of the actual tip–sample distance D. From such an experiment, the calculation of the tip–sample interactions is possible by reversing the integral in (5.4). As shown by Dürig [45], this results in

$$F_{\mathrm{ts}}^{\mathrm{la}}(D) = -\frac{\partial}{\partial D} \int_D^\infty \sqrt{2} \frac{c_z A^{3/2}}{f_0} \frac{\Delta f(z)}{\sqrt{z-D}}\,\mathrm{d}z, \quad (5.6)$$

allowing a direct calculation of the tip–sample interaction force from frequency shift vs. distance curves.

Application of this formula to the experimental frequency shift curves of Fig. 5.3a is shown in Fig. 5.3c. The obtained force curves are almost identical although obtained with different oscillation amplitudes. The fact that tip–sample forces (or, alternatively, potentials) can be determined with high accuracy and without the discontinuity due to the so-called *jump-to-contact* observed in conventional force curves [46] demonstrates the advantage of dynamic force spectroscopy compared to force–distance curves acquired without oscillating the cantilever.

As (5.4) was derived with the condition that the oscillation amplitude is considerably larger than the decay length of the tip–sample interaction, the same restriction applies to (5.6). However, using more complex algorithms, it is also possible to determine forces from dynamic force spectroscopy experiments without the restriction to large amplitudes. The numerical approach of

Gotsmann et al. [47,48], for example, works in every regime, as do the semi-analytical methods introduced by Dürig [49], Giessibl [50], and Pfeiffer [51]. The method of Sader and Jarvis [52], finally, results into the formula

$$F_{\mathrm{ts}}(D) = -\frac{\partial}{\partial D}\int_D^{\infty} \sqrt{2}\frac{c_z A^{3/2}}{f_0}\frac{\Delta f(z)}{\sqrt{z-D}} + 2c_z\frac{\Delta f}{f_0}(z-D) + \frac{c_z}{2}\frac{\Delta f}{f_0}\sqrt{\frac{A}{\pi}}\sqrt{z-D}\,\mathrm{d}z, \qquad (5.7)$$

which is easy to implement as an extension of (5.6) because only two additional terms have to be included into the integral. This equation is a good approximation for all amplitudes, but especially helpful if very small amplitudes are used such as it is frequently the case for quartz crystal sensors (see, e.g., [26,53–55]). Note that the numerical solution of (5.6) and (5.7) is greatly improved if the square-root singularity at the lower integration limit D of the denominator of the first term in the integral is eliminated by a change of variables $z \rightarrow D + t^2$ (see Chap. 4.4 in [56] for a discussion of this issue).

5.2.3 Extending Dynamic Force Spectroscopy to Three Dimensions

The above described concept can be extended to achieve three-dimensional force spectroscopy, that is, the probing and subsequent mapping of the complete force field above the sample surface [21]. As the acquisition of a three-dimensional force field with atomic resolution requires high stability, high lateral resolution, and high force sensitivity, a home-built low-temperature UHV force microscope optimized for atomic scale experiments was used to perform the experiment presented in this Sect. [40, 57]. In particular, low temperatures significantly reduce thermal drift and distortions due to piezo nonlinearities ("piezo creep").

Measurements were performed with a commercial single-crystalline silicon cantilever with an eigenfrequency of $f_0 = 195\,\mathrm{kHz}$ and a force constant of $c_z = 48\,\mathrm{N\,m^{-1}}$. After insertion into vacuum, the tip was first cleaned by argon ion sputtering to remove the silicon oxide layer and subsequently coated with an iron layer of 12.5 nm thickness by thermal evaporation. The sample was a nickel oxide single crystal, which had been cleaved in situ along its (001) plane. Note that due to NiO's rock salt structure, both atomic species (Ni and O) are present at the (001) surface.

To record a three-dimensional force field with atomic resolution on the lateral scale, the following procedure was applied. First, all scanning parameters, in particular the frequency shift Δf, were optimized to obtain atomic resolution during regular "topographic" imaging (acquisition of a plane of constant frequency shift). Immediately after scanning such an image, two times $32 \times 32 \times 256$ frequency shift values were captured in a box of $1 \times 1 \times 10\,\mathrm{nm^3}$ above the same scan area. The time needed to record this data set

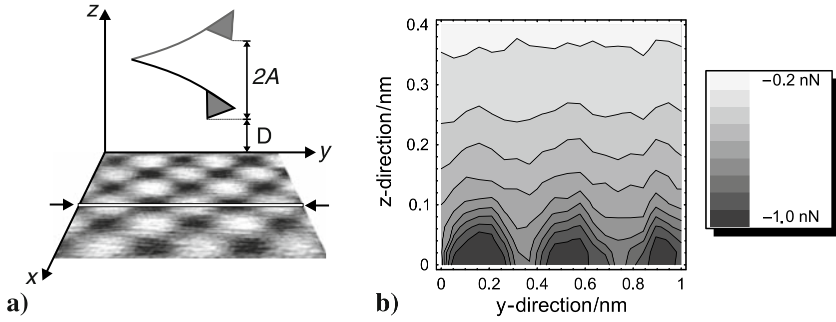

Fig. 5.4. The principle of 3D force spectroscopy, illustrated with the example of NiO (001). **(a)** The cantilever oscillates near the sample surface and measures the frequency shift at all locations defined by a dense raster grid inside an xyz box. The surface topography of the NiO sample, as obtained immediately before recording the spectroscopy field, is displayed in a perspective representation (image size: $10 \times 10\,\text{Å}^2$). **(b)** The reconstructed force field of NiO (001) taken along the line indicated in (**a**). The positions of the atoms are clearly visible

was about 80 min. Directly after recording this data array, a control image using the same scanning parameters in the constant frequency shift mode was acquired (see [22, 58] for details).

The data acquisition technique for the spectroscopy data array is schematically illustrated in Fig. 5.4a. A grid of equidistant points was defined at the scan area of $1 \times 1\,\text{nm}^2$. Using a specialized software routine, the procedure started in the lower left corner and continued line-by-line until the upper right corner was reached. At each grid position, the cantilever was first stabilized at a frequency shift of $\Delta f = -32.2\,\text{Hz}$, which had been set to obtain atomic resolution in Fig. 5.4a. The corresponding absolute z value was recorded to define an absolute z scaling. The cantilever was subsequently retracted by 9.80 nm from that point before it was approached by 9.93 nm ("trace") and retracted again ("retrace"). Consequently, the oscillating tip came nominally 130 pm closer to the sample surface at its point of closest approach during the recording of the topographic image of Fig. 5.4a. During both trace and retrace, 256 frequency shift values were recorded. After that, the cantilever was stabilized and moved to the next scan position, where the recording procedure was repeated. As a result, one obtains two $\Delta f(x, y, z)$ data arrays with $32 \times 32 \times 256$ frequency shift values, with each $\Delta f(x, y, z)$ array consisting of 1,024 individual $\Delta f(z)$ curves.

Using the method introduced earlier, it is now straightforward to determine the tip–sample interaction force F_{ts} from the $\Delta f(z)$-curves, that is, the $\Delta f(x, y, z)$ data array can be transformed into a $F_{\text{ts}}(x, y, z)$ force field. Figure 5.4b displays a two-dimensional cut along one scan line of the complete three-dimensional force field $F_{\text{ts}}(x, y, z)$ during retraction. This corresponds nearly to the crystallographic [100] direction. As the tip–sample distance is

stabilized at the same frequency shift $\Delta f = -32.2\,\mathrm{Hz}$ at every image point, the minimum tip–sample distance between the tip and an imaginary flat plane parallel to the surface is different at every image point. Therefore, the z scale of all curves within the line were adjusted with the recorded z position during stabilization at each image point. The lateral distances between the maxima in the force map are identical to those in Fig. 5.4a, that is, atomic resolution has been obtained close to the sample surface.

Considering the measurement procedure, it is clear that thermal and electronic drift can significantly distort the data. In fact, a detailed analysis [22,58] of the data set revealed that there was lateral drift of about one lattice constant in [110] direction during the experiment. This drift rate can be attributed to a slight temperature increase of $\approx 4\,\mathrm{mK\,h^{-1}}$ due to the slowly decreasing helium level in the bath cryostat. Moreover, electronic drift in the analogue electronics measuring the frequency shift resulted into a continuous drift of Δf of $-1.1\,\mathrm{Hz\,h^{-1}}$. Nonetheless, as the time needed to record a single $\Delta f(z)$ curve ($\approx 2.4\,\mathrm{s}$) or a complete scan line of curves ($\approx 150\,\mathrm{s}$ per line) is comparatively short, the amount of drift within one line is negligible.

5.3 Force Field Spectroscopy on Ionic Crystals

5.3.1 Force Fields and Energy Dissipation on NaCl

As shown earlier, the systematic mapping of tip–sample forces as a function of the tip position in three dimensions requires great experimental efforts. Most importantly, drift rates must be exceptionally low if a large number of individual force curves should be collected within a single experiment, which usually is only possible with intricate AFM set-ups operating at low temperature. We will show in this section that the 3D force spectroscopy technique can nevertheless be employed at room temperature with atomic precision, thus opening up its possibilities to a large community of scientists and engineers. Prerequisite for a successful application, however, is that the number of curves collected overall is relatively low so that the measurement is completed on a time scale faster than typical drift rates. Here we focus on ionic crystals and in particular NaCl, as single crystals of this material proved to be well suited for atomic-scale investigations under ultrahigh vacuum conditions [59, 60].

Experiments were performed with an ultrahigh vacuum AFM operated at room temperature [23]. Prior to the collection of the force curves, the tip was intentionally brought several times into intimate contact with the surface. This procedure most likely resulted in a tip with an NaCl cluster termination [16]. An atomic resolution topographic image of the NaCl surface is shown in Fig. 5.5. On a surface area of $2 \times 2\,\mathrm{nm}^2$, 3D force mapping was performed as described in the previous section by measuring the force-induced frequency shift as a function of relative tip–sample distance z on a predefined

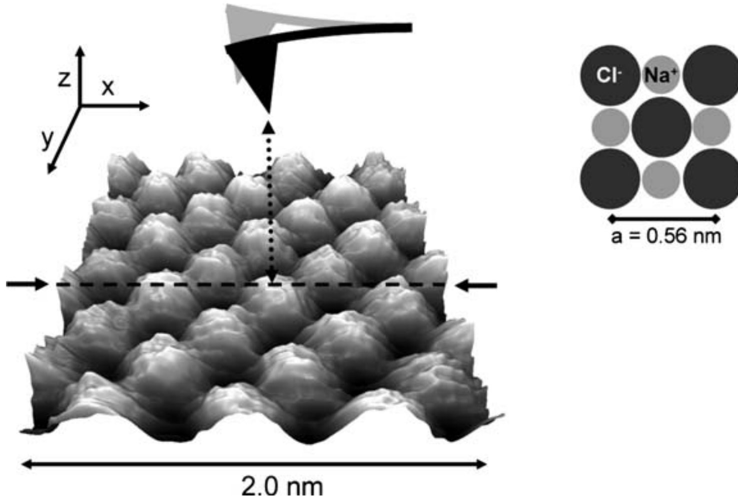

Fig. 5.5. Grayscale height image showing the surface topography (raw data) at a constant frequency shift of $\Delta f = -138\,\text{Hz}$ obtained in conventional scan mode of NC-AFM on NaCl (100) in ultrahigh vacuum with an oscillation amplitude of $A = 4.5\,\text{nm}$. For the subsequent 3D spectroscopy, the frequency shift was acquired as a function of tip–sample distance z for 34 points along the x direction and for 10 equidistant y positions. The force map analysis described below was performed for a y position along the *dashed line*. Inset in the upper right corner: The NaCl (001) surface

grid, consisting of 34 equidistant points along the x axis for 10 equidistant positions along the y axis.

Figure 5.6a shows the resulting raw data image of the frequency shift as a function of the vertical tip–sample distance and the lateral x position along the dashed line shown in Fig. 5.5, thus representing one slice in real space. The circular areas at around $z = 0.22\,\text{nm}$ indicate the molecular lattice sites, separated by the NaCl lattice constant of 0.56 nm. For further reference, we distinguish the two atomic sites in the center of the circles and in between the circles, which correspond to the lattice positions of the two ionic species of NaCl, by referring to them as A and B sites, respectively (cf. Fig. 5.6).

Simultaneously with the frequency shift, the dissipated energy was measured (see Fig. 5.6 b), which shows atomic-scale contrast only at distances of $z < 0.2\,\text{nm}$. As stable feedback operation during scanning is usually restricted to the parts of the frequency shift curves with positive slope (i.e., the frequency shift becomes more positive with increasing tip-sample distance), atomic contrast in the dissipation develops here only far beyond the point of stable scan operation. This shows that interpretation of atomic-scale contrast in energy dissipation images must carefully consider the influence of the distance control loop.

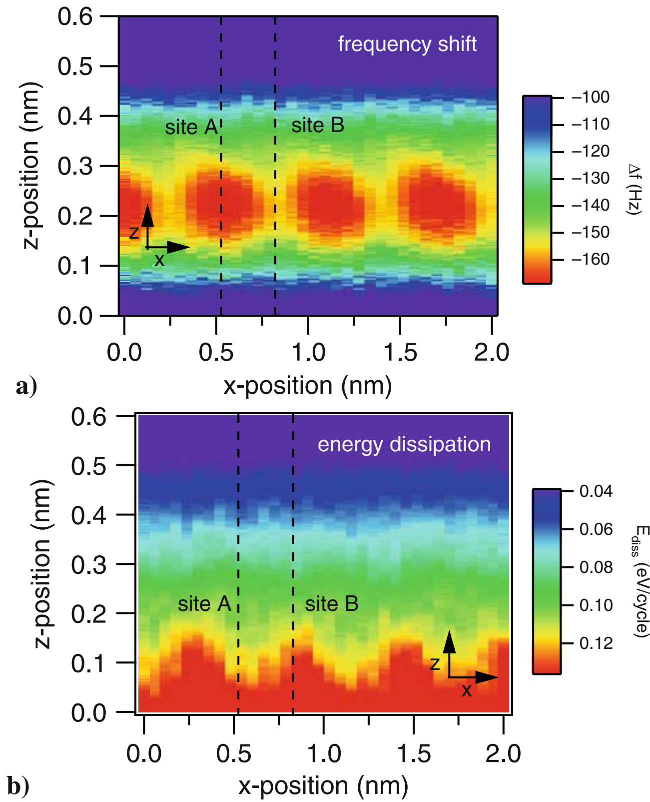

Fig. 5.6. (a) Plot showing the measured frequency shift Δf (unprocessed raw data) as a function of both the horizontal position along the x axis as well as the relative tip–sample separation z. The image comprises 34 spectroscopy curves, each covering a range of $\Delta z = 1.1\,\text{nm}$. Long-range force interactions were measured up to distances of $z = 3\,\text{nm}$. **(b)** Simultaneously acquired "dissipation map," featuring the energy that is dissipated per oscillation cycle

The tip–sample interaction potential energy map calculated from the frequency shift curves [45] is presented in Fig. 5.7a. The image shows the exact position and quantitative values for the potential energy minima, which are not only relevant for surface diffusion processes [29, 61], but also for atomic-scale friction models. According to the Prandtl–Tomlinson model [62, 63], the tip is trapped in the local energy minima of a sinusoidal interaction potential corresponding to site A. Upon lateral movement of the tip base, the tip apex will move sidewards either in a discontinuous stick-slip motion or by smoothly following the potential profile; which motion will be realized depends mainly on the ratio between the stiffness of the tip–surface contact and the height of the energy barrier [60].

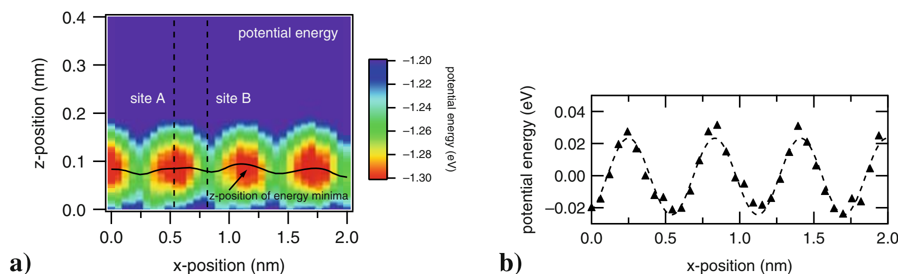

Fig. 5.7. (a) Image of the tip–sample potential energy as a function of horizontal and vertical tip position. The *solid black line* indicates the z positions of the potential energy minima. **(b)** Plot of the experimental values of the potential energy (*triangles*) collected along the black line in (**a**), recalibrated so that the average energy is zero. Their values can be approximated by a sinusoidal curve (*dashed line*), yielding an effective potential energy barrier of $\Delta E_{\text{barrier}} = 48\,\text{meV}$

The equilibrium z position of the tip atom is in the minimum of the individual $E(z)$ curves, indicated by the black solid line in Fig. 5.7a. Those minima are almost independent of the x position of the tip, showing only a small corrugation of 10 pm. Considering a lateral displacement of the tip base, the tip apex atom would be dragged along the potential minima (Fig. 5.8) and experience the strongly varying potential energy depicted in Fig. 5.7b. From this energy profile, we can directly determine the effective energy barrier $\Delta E_{\text{barrier}} = 48\,\text{meV}$, which is the fundamental parameter in atomic friction models [62–65]. From atomic-scale friction experiments, effective energy barriers in the range from 0.1 to 0.5 eV have been reported on NaCl crystals [60] depending on the applied effective load. The above value represents the potential energy barrier experienced by a single atom terminated tip apex, as opposed to the multiatom contacts typically encountered in conventional friction force experiments. Interestingly, the shape of the potential energy barrier in Fig. 5.7b is well described by a sinusoidal curve (*dashed line*), which is often assumed in simple atomic friction models, but has been questioned lately [66] in the analysis of friction experiments on mica surfaces.

Those energy barriers are comparable to typical diffusion energy barriers determined from the dynamics of surface adsorbates [29, 61]. The experimentally determined effective energy barrier suggests a considerable mobility of adsorbates on an NaCl surface at room temperature, which is in fact observed experimentally. However, one has to keep in mind that the tip atom is connected to a large tip base, which might influence the overall mechanical behavior of the contact. In fact, evidence for the complex mechanical behavior of the investigated single-atom contact can be derived from the following analysis of the tip–sample forces.

For a more detailed analysis of the interaction forces acting in z direction, we turn to Fig. 5.9a, which shows the vertical force map calculated from

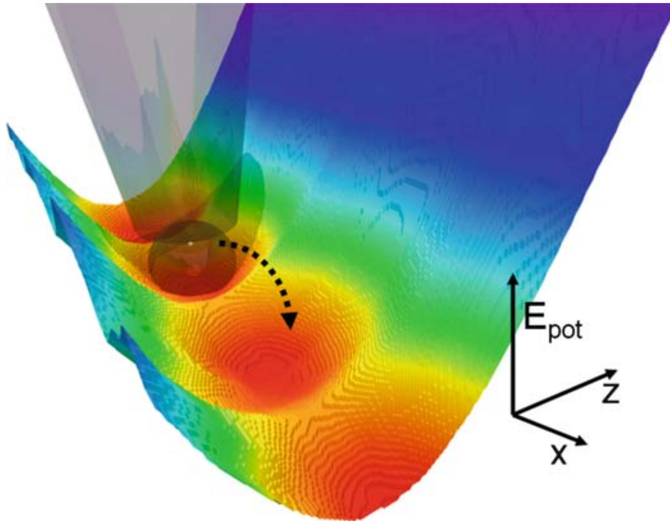

Fig. 5.8. Figure showing a 3D representation of the interaction energy map, visualizing the local energy minima. The last tip atom, which would jump from minimum to minimum during a lateral sliding movement along the x axis (*dashed arrow*), is represented by a *grey sphere*

the potential energy map by taking the partial derivative $F_{\text{vertical}}(z,x) = -\frac{\partial E(z,x)}{\partial z}$. The onset of repulsive forces is characterized by a minimum in the force curves [67], emphasized by the black circles in the force map. In contrast to the energy map, the force map shows two distinct minima per lattice constant, corresponding to the two ionic species in the NaCl crystal. From the potential energy map we can also deduce the lateral force map by taking the partial derivative with respect to the horizontal axis $F_{\text{lateral}}(z,x) = -\frac{\partial E(z,x)}{\partial x}$. The resulting force map in Fig. 5.9 b shows no significant lateral forces for tip–sample distances larger than $z = 0.37\,\text{nm}$. Below this distance, the lateral forces reach values up to 40 pN in both directions, pointing towards the energy minima.

In Fig. 5.10a, the vertical (i.e., normal) forces are shown as a function of tip–sample distance above site A and site B. While the repulsive force part of curve A shows a monotonically increasing characteristic with an effective contact stiffness of $3.2\,\text{Nm}^{-1}$, force curve B shows a transition point at $F_{\text{trans}} = -0.34\,\text{nN}$, where the curve is horizontally shifted. After this transition point curves A and B become almost identical. This transition is reminiscent of load relaxations due to defect creation in a subsurface volume during nanoindentation experiments [68, 69]. In this case, the mechanical relaxation most likely takes place at the tip apex. Without an additional compliant mechanism, the repulsive part of the force curve B would continuously increase, as for instance the dashed curve shows, which we refer to as the unrelaxed site B

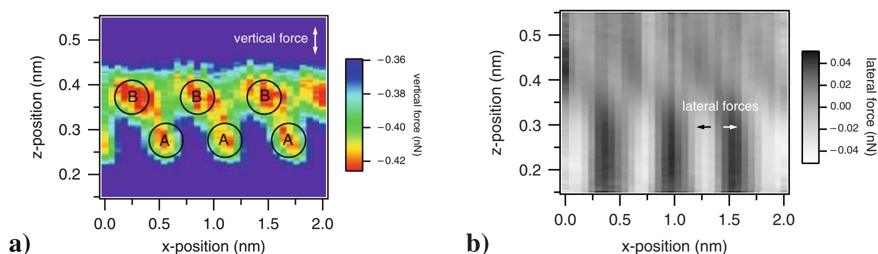

Fig. 5.9. (a) Image showing the force acting in the vertical z direction (i.e., the normal force) as a function of both the x and z position of the tip. The onset of repulsive forces is at different vertical and horizontal positions for the two ionic species (*black circles* at the site A and site B positions). **(b)** The lateral forces as a function of x and z position of the tip derived from the potential energy diagram. The maximum lateral forces reach values of 40 pN

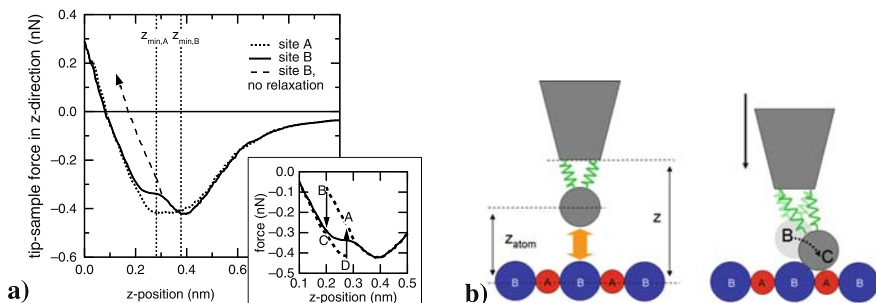

Fig. 5.10. (a) Normal forces as a function of relative tip–sample distance z taken at the x positions labeled A and B. The *dashed curve* was constructed for the purpose of demonstration from the left part ($z < 0.2$ nm) of the solid curve, shifted by 0.9 nm to the right. The inset shows the experimental site B force (*solid*) compared with the force curves expected from a double well potential energy model (*dotted*), indicating the resulting hysteresis due to different forces during the forward and backward movement of the oscillating tip. **(b)** *Left*: Tip atom approaching site B of the surface. *Right*: Beyond a certain distance the tip atom relaxes towards site A, which is represented by the sudden force drop from B to C in the inset of (**a**)

curve. As the precise atomic configuration of the tip and the sample remains unchanged, as evidenced by the reproducibility of the subsequent force curves, the mechanical relaxation at the tip–sample interface must be fully reversible.

A simple model of the single atom contact is used to rationalize this observation: the tip apex is modeled by a stiff tip base with one atom connected by effective vertical and horizontal springs, while the surface consists of a periodic arrangement of the two ionic species, which are considered infinitely stiff (see Fig. 5.10b). The mechanical stiffness of the tip base was calculated by a finite element simulation using FEMlab, where the tip was approximated by a silicon cone of height 200 nm with an apex radius of $R = 4$ nm and a half

opening angle of 10°. The resulting compliances were $c_{\text{vertical}} = 37\,\text{N}\,\text{m}^{-1}$ and $c_{\text{lateral}} = 8.8\,\text{N}\,\text{m}^{-1}$, and therefore indicating that the tip base can be regarded as stiff in comparison to the experimentally observed force gradients for the vertical and lateral tip–sample interaction.

When approaching the tip above site A, the repulsive forces will compress mainly the effective vertical spring. Above site B, however, the lateral compliance of the tip apex atom will lead to a mechanical relaxation of the tip apex atom away from site B towards site A, which occurs at the transition force F_{trans}. The emergence of a tip atom relaxation also explains the different image contrast in the energy and force maps, yielding one and two minima per lattice constant, respectively. The minima in the energy map represent the total energy minimum, taking into account the mechanical tip atom relaxation. The force minima, on the other hand, are characterized by the onset of repulsive forces, where the relaxation has not yet occurred, therefore clearly indicating separate minima at both sublattice sites.

Because the tip is oscillating in DFS, the measured forces are an average of the forces acting during the forward and backward movement (cf. Sect. 5.2.2). During the forward cycle, the force will follow the dashed curve until a threshold force is reached. Then the curve will drop vertically to the shifted curve, as the atom suddenly relaxes to its new position while the tip base position stays constant. This behavior is sketched in the inset of Fig. 5.10a (dotted curve) by the vertical transition from B to C. During the retraction cycle, the tip atom will jump back to the initial force curve at a different position as before (from D to A), and a hysteresis develops.

The best agreement for the instability position predicted by the energy diagram with the experimentally observed transition point B to C is obtained by adjusting the only left unknown parameter $c_{\text{lateral}} = 0.4 \pm 0.1\,\text{N}\,\text{m}^{-1}$. This value coincides with a typical lateral contact stiffness obtained from atomic scale friction experiments [60]. A comparison of the effective experimental force curve, which is inherently an average of the forward and backward movement of the tip during the oscillation cycle, and the corresponding predicted hysteresis loop is shown in the inset of Fig. 5.10a. This should leave a significant fingerprint in the energy dissipation [70, 71]. The dissipation map in Fig. 5.6b shows enhanced values exactly at the B sites, with contrast developing beyond the transition point ($z < 0.2\,\text{nm}$), in excellent agreement with the simple model. The above analysis demonstrates that force field spectroscopy with simultaneous measurement of conservative and dissipative is a powerful technique to understand mechanical relaxation processes at the atomic level.

5.3.2 Force Vector Fields on KBr

We have seen above that not only normal forces but also the forces acting horizontally along the specific direction that the xz map is following can be derived. By superposition of theses vertical and lateral atomic force fields, a vector field can be constructed that represents the magnitude and direction of

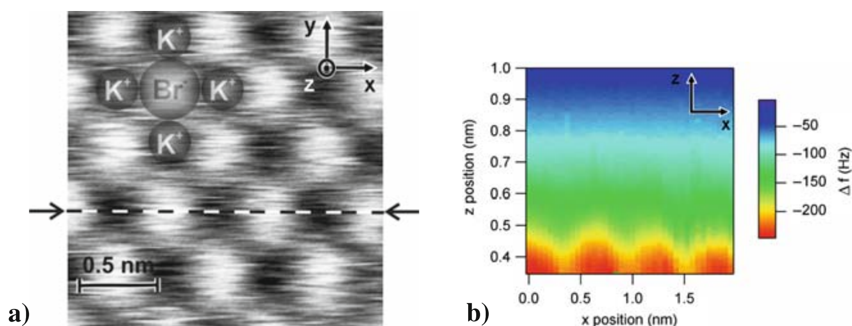

Fig. 5.11. (a) Surface topography of a KBr (001) sample. The overlay indicates the positions of K^+ and Br^- surface ions as they have been determined by the force field analysis. The *dashed line* marks a representative y position along the sites of topography maxima at which the force field measurements were performed. **(b)** Measured frequency shift (unprocessed raw data) displayed as a function of the relative tip–sample distance z and the horizontal tip position along the x axis. Each of the 38 individual Δf curves comprised in this plot covers a distance of 0.65 nm in z direction

forces acting between the terminating tip apex atom and the surface atoms as a function of their relative position in real space. This ability is illustrated in this section with the example of a KBr (001) single crystal that was cleaved in situ to assure an atomically clean surface and heated to 420 K for 60 min to equilibrate residual charges. The measurements were carried out with the same system as described earlier.

Figure 5.11a shows an atomically resolved area of $2 \times 2\,\text{nm}^2$ on the KBr (001) surface. To obtain the vertical force field, the frequency shift was measured as a function of the relative tip–sample distance on a grid of 38 equally spaced points in the x and 6 equidistant positions in the y direction. Before and after each individual frequency shift vs. distance measurement, the feedback loop (keeping the frequency shift constant by adjusting the tip–sample distance) was switched on to stabilize the system at a reference tip–sample distance for 104 ms. The frequency shift was measured over a range of 1.1925 nm in steps of 0.0025 nm with a time constant of 5.12 ms for each data point. Together with the time needed for feedback stabilization, this resulted in a total acquisition time of 1.7 min per x-z slice. Positional drift during these room temperature measurements was $\approx 0.001\,\text{nm}\,\text{s}^{-1}$, which is negligible in the z direction, as the z position is stabilized by the feedback every 2.44 s. In lateral direction, this drift amounts to an uncertainty in the y position of one slice of 0.1 nm.

A two-dimensional map shows the unprocessed frequency–distance data as a function of lateral and vertical tip position along the corrugation maxima (Fig. 5.11b). The individual force curves, which were calculated from the frequency shift curves, in Fig. 5.12a contain the site-specific forces that are

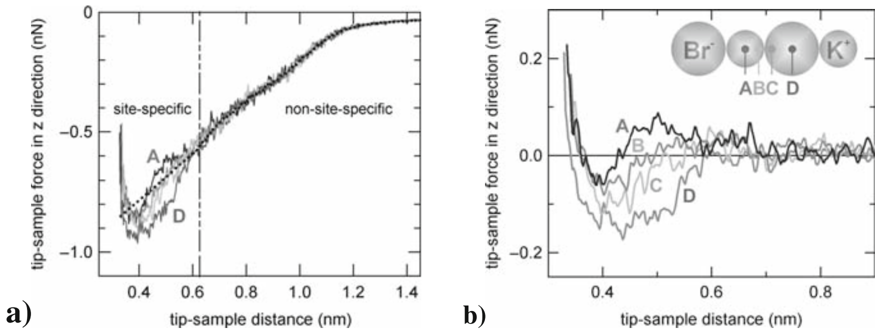

Fig. 5.12. (a) Experimental force curves recorded on KBr (001) along a line between the positions of the two ionic species; the exact lattice positions are labeled A–D in the inset in (**b**). The *black dotted curve* represents the average over all force curves with a linear extrapolation into the regime of site specific behavior. **(b)** Site-specific part of the short-range regime for the same force curves as in (**a**), where the nonsite-specific contributions have been subtracted

responsible for the atomic scale image contrast as well as site-independent long range forces. The latter typically is a superposition of van der Waals and electrostatic forces, whereas the site-specific part is dominated by short-range chemical binding forces. The forces on different lattice sites labeled A–D along a line between the two ionic species in Fig. 5.12a match within the noise up to $z = 0.62\,\text{nm}$, while site-specific differences occur in the range $0.30\,\text{nm} < z < 0.62\,\text{nm}$. The precise force law for the nonsite-specific force contribution is unknown, but those forces are sufficiently well approximated by a line fit for $0.62\,\text{nm} < z < 1.10\,\text{nm}$, which can be extrapolated into the site-specific regime. This first-order approximation is justified as any long-range background force is expected to show a continuous curve shape and should not contribute to atomic scale features. Figure 5.12b shows the resulting short range forces, which was derived by subtracting the dotted curve (i.e., nonsite-specific forces) from the experimental force curves.

The corresponding site-specific vertical force field is illustrated in Fig. 5.13a, which is based on 23 adjacent force curves. The areas of attractive forces up to $F = -0.18\,\text{nN}$ at the x position of one ionic species on the surface show a roughly triangular shape in the force map. In between the attractive force areas, we find small circularly shaped areas with repulsive forces up to $F = 0.07\,\text{nN}$ around $z = 0.50\,\text{nm}$ at the location of the oppositely charged surface ion. In fact, the direct comparison of these experimental force maps with simulated force maps revealed excellent quantitative agreement for the case of a K^+ terminated tip [33].

In a next step, the lateral tip–sample forces were calculated from the force fields by integration in z direction and subsequent differentiation in x direction [22, 24]. Combining the vertical and lateral forces allows one to extract the corresponding force vectors in the x-z plane. Those vectors quantify

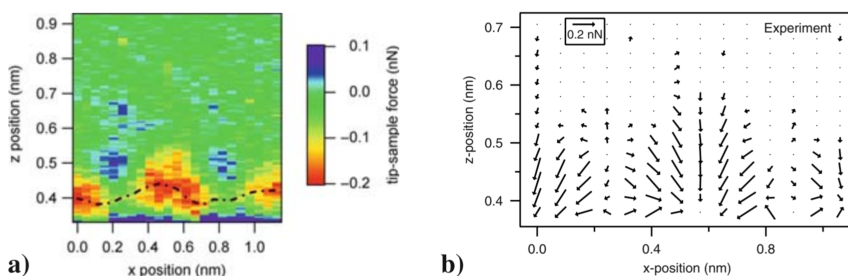

Fig. 5.13. (**a**) The two-dimensional map of the site-specific vertical tip–sample forces. (**b**) Atomic scale force vector field on KBr (001) determined from the AFM experiment. Individual arrow length and orientation represents the magnitude and direction of the site-specific force experienced by the atomically sharp tip at the respective position in the x-z plane

magnitude and direction of the site-specific force experienced by an atomically sharp tip at the respective position in the x-z plane above the surface. Figure 5.13b shows the resulting experimental force vector field. The force vector maps show that approaching the tip directly above a K^+ ion leads to no lateral forces, whereas the lateral forces are strongest at the position between the K^+ and the Br^- sample ions, always pointing towards the Br^- ion. This is a direct consequence of the local energy minimum of the tip–sample system at the Br^- sites.

5.4 True 3D Force Field Spectroscopy on Graphite

We have seen in the previous chapter that even though impressive results can be obtained with 3D force field spectroscopy performed at room temperature, the number of force curves that can practically be acquired within a single experiment is limited to a couple of hundred individual curves due to thermal drift. Therefore, 3D resolution in such measurements is usually poor, and experimentalist focus on collecting individual xz planes as shown above rather than full dense (x, y, z, F_{ts}) data sets. However, xy force maps featuring directly tip–sample interaction forces or potential energies instead of the "planes of constant frequency shift" that regular "topographic" NC-AFM imaging delivers would be highly beneficial for many applications. This is because constant-frequency shift images are difficult to interpret, while force and energy fields can be directly understood and compared to theory.

In this section, we are reporting results that comprise 256×119 pixels laterally, equivalent to the acquisition of 30,464 $\Delta f(z)$ curves. The original data presented in this section has been published in [34]. Overall, one pixel was recorded every 6.8 pm laterally and $\approx$2 pm vertically, resulting in a covered xy area of $1{,}750 \times 810\,\text{pm}^2$. Key for the successful acquisition of this data in such a dense grid, which took 40 h to complete, were two main components:

first, the use of a home-built high-resolution, low drift microscope operating in ultrahigh vacuum ($p \approx 4 \times 10^{-11}$ mbar) and at low temperatures ($T \approx 6$ K), which showed drift rates as low as one unit cell per day once in equilibrium [26]. Second, by carefully characterizing the thermal drift during data acquisition, we were able to remove the remaining drift after the data acquisition had been completed. This resulted in a virtually drift-free array of (x, y, z, F_{ts}) data despite much higher pixel density and much longer measurement times than demonstrated in the above sections. In addition, the potential energy E, the energy dissipated during an individual oscillatory cycle E_{diss}, and the tunneling current I have been recorded simultaneously. As a consequence, cuts along *any plane* within the covered 3D space (including xy planes) can be produced, delivering high-resolution maps of F_{ts}, E, E_{diss}, and I from any angle. Details on the data acquisition and analysis procedures have been described in [35].

The experiments presented here were performed on highly oriented pyrolytic graphite (HOPG). The sample was cleaved in air, transferred into vacuum, and heated to 450 K for 30 min before being moved into the microscope. The microscope's force sensor was a quartz tuning fork in the so-called Q-plus configuration [53], featuring an eigenfrequency and quality factor of f_0=29,023 Hz and $Q \approx$21,000, respectively. Oscillation amplitude was 0.23 nm.

Visualizations of the full 3D data sets for the normal force (a), potential energy (b), and energy dissipated during an individual oscillation cycle (c) are displayed in Fig. 5.14. The z axis was arbitrarily calibrated to be zero at the height given by the lowest plane that has been recorded during data acquisition, and so z values do not directly coincide with an absolute distance from the surface. The arrays shown are cut off at about 0.3 nm height although the full sets cover 3.5 nm in that direction, as the data does not include any lateral contrast for larger distances. To increase the contrast for the eye, the average force/energy in each plane of constant z was subtracted for all diagrams, rendering the atomic-scale contrast clearly visible. Note that the force corrugation caused by the atoms, for example, is only about 3% of the total force acting on the tip (the maximum attractive force measured between tip and sample was about -2.34 nN at the distance of closest approach).

Having full 3D data available, it is possible to produce actual force images on the atomic scale. Figure 5.15a, b show force images at 7 pm (a) and 44 pm (b) above the plane of closest approach. With these images and the dozens of images that can be generated at intermediate heights, it can be studied how the contrast changes with distance, giving valuable insight into the strength of local interactions. By an analysis presented elsewhere [34], the positions of all atoms in the lattice can be determined, as indicated by the hexagon in Fig. 5.15a, b.

Other useful information can be drawn from vertical force maps, which illustrate how the force field of individual atoms extends into vacuum. Figures 5.15c–e show three examples of such plots, which have been recorded within the area marked by the grey rectangle in Fig. 5.15a. It is especially

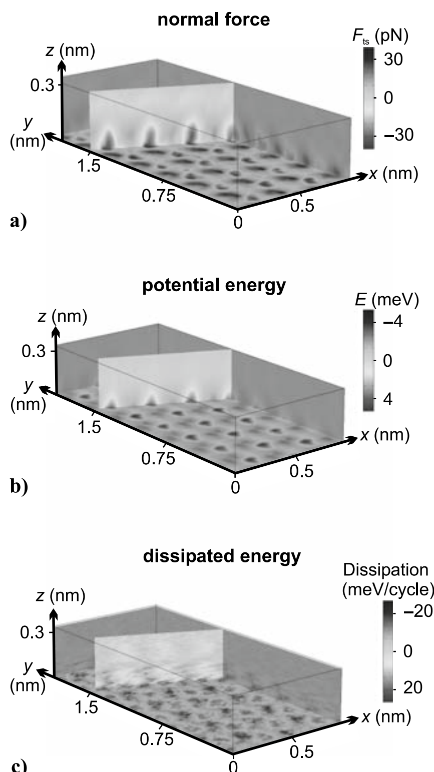

Fig. 5.14. Representations of the three-dimensional data sets for the normal tip–sample interaction force F_{ts} **(a)**, the tip–sample potential energy E **(b)**, and the energy dissipated per cycle E_{diss}**(c)** recorded on graphite. The average force/energy was removed in each plane of constant z to make the respective atomic-scale contrasts visible. To highlight the fact that full 3D data is available and cuts in any direction can be produced, a plane normal to the surface along a row of maxima has been included in the figure. In this projection, it can be seen how the force and energy fields extend into vacuum

interesting to note that in Fig. 5.15c, the positions of the force maxima are changing with the height. However, this is not visible in the other cuts.

The ability to collect $(x, y, z, F_{\mathrm{ts}})$ arrays in such a dense raster and virtually drift-free opens the door to analyze more effects on the atomic scale than ever before. It might find application in all fields of science where site-specific atomic-scale information on interaction forces and potential energies is important, such as chemical imaging, catalysis, thin film growth, device fabrication, or nanotribology. Not only height-dependent changes on the atomic scale can be made visible, but also changes between "regular" tips and tips that are functionalized with specific atomic species of molecules to show enhanced reactivity with the surface. Such information might be very helpful as input for improving theoretical models and to verify numerical analysis.

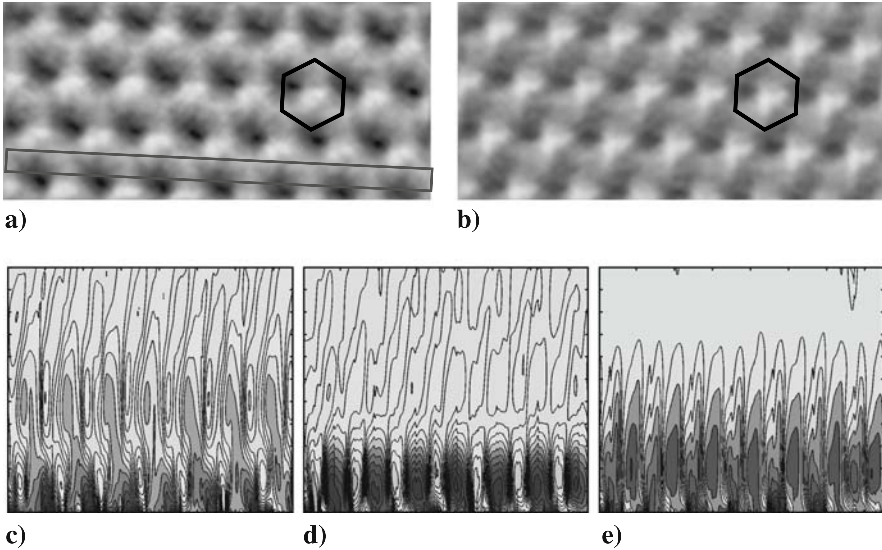

Fig. 5.15. Different slices of the force data set shown in Fig. 5.14a. (**a**) and (**b**): Force images for different heights above the surface: (**a**) 7 pm above lowest imaged plane, (**b**) 44 pm above lowest imaged plane. Image sizes are 1,750 pm × 810 nm. In contrast to conventional "topographical" NC-AFM images, which show planes of constant frequency shift, the contrast in the images is given by the actual force acting between tip and sample at the specific height indicated above. The corrugation in (**a**) is about 60 pN and in (**b**) about 40 pN. (**c**)–(**e**): Vertical force maps projected (roughly) onto the xz plane taken at three different locations within the *grey rectangle* given in (**a**). Note that the precise orientation relative to the lattice as given by the rectangle includes a rotation by about 15° relative to the xz plane to be in line with rows of force maxima. To enhance contrast, the average force was removed for each height z as described earlier for Fig. 5.14a. Map sizes are x by z 1,750 × 220 pm^2 each, and the force scale spreads from −30 to +30 pN

Acknowledgements

The authors thank all colleagues who contributed to this work with their experimental results: Wolf Allers, Shenja Langkat, and Alexander Schwarz (University of Hamburg), Domenique Weiner and Kai Ruschmeier (University of Münster), as well as Boris J. Albers, Mehmet Z. Baykara, Todd C. Schwendemann, and Nicolas Pilet (Yale University). A. S. acknowledges financial support from the Deutsche Forschungsgemeinschaft (DFG SCHI 619/1-2 and TRR 61 project B7), U. S. from the National Science Foundation (grant No. MRSEC DMR 0520495), the Department of Energy (grant No. DE-FG02-06ER15834), and the Petroleum Research Fund (grant No. 42259-AC5).

References

1. G. Binnig, C.F. Quate, C. Gerber, Phys. Rev. Lett. **56**, 930 (1986)
2. T.R. Albrecht, P. Grütter, D. Horne, D. Rugar, J. Appl. Phys. **69**, 668 (1991)
3. F.J. Giessibl, Science **267**, 68 (1995)
4. S. Orisaka, T. Minobe, T. Uchihashi, Y. Sugawara, S. Morita, Appl. Surf. Sci. **140**, 243 (1999)
5. C. Loppacher, M. Bammerlin, M. Guggisberg, S. Schär, R. Bennewitz, A. Baratoff, E. Meyer, H.-J. Güntherodt, Phys. Rev. B **62**, 16944 (2000)
6. V. Caciuc, H. Hölscher, D. Weiner, H. Fuchs, A. Schirmeisen, Phys. Rev. B **77**, 045411 (2008)
7. S. Kitamura, M. Iwatsuki, Jpn. J. Appl. Phys. **34**, L145 (1995)
8. H. Ueyama, M. Ohta, Y. Sugawara, S. Morita, Jpn. J. Appl. Phys. L **34**, 1086 (1995)
9. Y. Sugawara, M. Ohta, H. Ueyama, S. Morita, Science **270** 1646 (1995)
10. A. Schwarz, W. Allers, U.D. Schwarz, R. Wiesendanger, Phys. Rev. B **61**, 2837 (2008)
11. M. Bammerlin, R. Lüthi, E. Meyer, A. Baratoff, J. Lü, M. Guggisberg, C. Gerber, L. Howald, H.-J. Güntherodt, Probe Microsc. **1**, 3 (1997)
12. W. Allers, A. Schwarz, U.D. Schwarz, R. Wiesendanger, Europhys. Lett. **48**, 276 (1999)
13. C. Barth, M. Reichling, Nature **414**, 54 (2001)
14. R. Hoffmann, M.A. Lantz, H.J. Hug, P.J.A. van Schendel, P. Kappenberger, S. Martin, A. Martin, A. Baratoff, H.-J. Güntherodt, Phys. Rev. B **67**, 085402 (2003)
15. M.A. Lantz, H. Hug, R. Hoffmann, P.J.A. van Schendel, P. Kappenberger, S. Martin, A. Baratoff, H.-J. Güntherodt, Science **291**, 2580 (2001)
16. R. Hoffmann, L.N. Kantorovich, A. Baratoff, H.J. Hug, H.-J. Güntherodt, Phys. Rev. Lett. **92**, 146103 (2004)
17. M. Abe, Y. Sugimoto, O. Custance, S. Morita, Appl. Phys. Lett. **87**, 173503 (2005)
18. S. Hembacher, F.J. Giessibl, J. Mannhart, C.F. Quate, Phys. Rev. Lett. **94**, 056101 (2005)
19. Y. Sugimoto, S. Innami, M. Abe, O. Custance, S. Morita, Appl. Phys. Lett. **91**, 093120 (2007)
20. Y. Sugimoto, P. Pou, M. Abe, P. Jelinek, R. Perez, S. Morita, O. Custance, Nature **446**, 64 (2007)
21. H. Hölscher, S.M. Langkat, A. Schwarz, R. Wiesendanger, Appl. Phys. Lett. **81**, 4428 (2002)
22. A. Schwarz, H. Hölscher, S.M. Langkat, R. Wiesendanger, AIP Conf. Proc. **696**, 68 (2003)
23. A. Schirmeisen, D. Weiner, H. Fuchs, Phys. Rev. Lett. **97**, 136101 (2006)
24. M. Abe, Y. Sugimoto, T. Namikawa, K. Morita, N. Oyabu, S. Morita, Appl. Phys. Lett. **90**(20), 203103 (2007)
25. M. Heyde, G.H. Simon, H.P. Rust, H.J. Freund, Appl. Phys. Lett. 263107 (2006)
26. B.J. Albers, M. Liebmann, T.C. Schwendemann, M.Z. Baykara, M. Heyde, M. Salmeron, E.I. ALtman, U.D. Schwarz, Rev. Sci. Instrum. **79**, 033704 (2008)
27. M. Ternes, C.P. Lutz, C.F. Hirjibehedin, F.J. Giessibl, A.J. Heinrich, Science **319**, 1066 (2008)

28. M. Ashino, D. Obergfell, M. Haluska, S. Yang, A.N. Khlobystov, S. Roth, R. Wiesendanger, Nat. Nanotechnol. **3**, 337 (2008)
29. R. Gomer, Rep. Prog. Phys. **53**, 917 (1990)
30. E.W. Müller, Ergebn. exakt. Naturwiss. **27**, 290 (1953)
31. E.W. Müller, Z. Phys. **131**, 136 (1951)
32. G. Binnig, H. Rohrer, C. Gerber, E. Weibel, Phys. Rev. Lett. **49**(1), 57 (1982)
33. K. Ruschmeier, A. Schirmeisen, R. Hoffmann, Phys. Rev. Lett. **101**, 156102 (2008)
34. B.J. Albers, T.C. Schwendemann, M.Z. Baykara, N. Pilet, M. Liebmann, E.I. Altman, and U.D. Schwarz, Nat. Nanotechnol. **4**, 307 (2009)
35. B.J. Albers, T.C. Schwendemann, M.Z. Baykara, N. Pilet, M. Liebmann, E.I. Altman, and U.D. Schwarz, Nanotechnol. **20**, 264002 (2009)
36. Q.D. Zhong, D. Inniss, K. Kjoller, V.B. Elings, Surf. Sci. Lett. **290**, L688 (1993)
37. P.K. Hansma, J.P. Cleveland, M. Radmacher, D.A. Walters, P.E. Hillner, M. Bezanilla, M. Fritz, D. Vie, H.G. Hansma, C.B. Prater, J. Massie, L. Fukunaga, L. Gurley, V.B. Elings, Appl. Phys. Lett. **64**, 1738 (1994)
38. C.A.J. Putman, K.O. Vanderwerf, B.G. Degrooth, N.F. Vanhulst, J. Greve, Appl. Phys. Lett. **64**, 2454 (1994)
39. H. Ueyama, Y. Sugawara, S. Morita, Appl. Phys. A **66**, S295 (1998)
40. W. Allers, A. Schwarz, U.D. Schwarz, R. Wiesendanger, Rev. Sci. Instrum. **69**, 221 (1998)
41. F.J. Giessibl, Phys. Rev. B **56**, 16010 (1997)
42. H. Hölscher, B. Gotsmann, W. Allers, U.D. Schwarz, H. Fuchs, R. Wiesendanger, Phys. Rev. B **64**, 075402 (2001)
43. H. Hölscher, B. Gotsmann, A. Schirmeisen, Phys. Rev. B **68**, 153401 (2003)
44. R.H. Simon, M. Heyde, H.P. Rust, Nanotechnology **18**, 255503 (2007)
45. U. Dürig, Appl. Phys. Lett. **75**, 433 (1999)
46. Y. Seo, W. Jhe, Rep. Prog. Phys. **71**, 016101 (2008)
47. B. Gotsmann, B. Ancykowski, C. Seidel, H. Fuchs, Appl. Surf. Sci. **140**, 314 (1999)
48. B. Gotsmann, H. Fuchs, Phys. Rev. Lett. **86**, 2597 (2001)
49. U. Dürig, Appl. Phys. Lett. **76**, 1203 (2000)
50. F.J. Giessibl, Appl. Phys. Lett. **78**, 123 (2001)
51. O. Pfeiffer, Quantitative dynamische Kraft- und Dissipationsmikroskopie auf molekularer Skala. Ph.D. thesis, Universität Basel, 2004
52. J.E. Sader, S.P. Jarvis, Appl. Phys. Lett. **84**, 1801 (2004)
53. F.J. Giessibl, Appl. Phys. Lett. **73**, 3956 (1998)
54. J. Jersch, T. Maletzky, H. Fuchs, Rev. Sci. Instrum. **77**, 083701 (2006)
55. M. Heyde, M. Kulawik, H.P. Rust, H.J. Freund, Rev. Sci. Instrum. **74**, 2446 (2006)
56. W.H. Press, S.A. Tekolsky, W.T. Vetterling, B.P. Flannery, *Numerical Recipes in C* (Cambridge University Press, Cambridge, 1992)
57. A. Schwarz, U.D. Schwarz, S. Langkat, H. Hölscher, W. Allers, R. Wiesendanger, Appl. Surf. Sci. **188**, 245 (2002)
58. S.M. Langkat, H. Hölscher, A. Schwarz, R. Wiesendanger, Surf. Sci. **527**, 12 (2003)
59. E. Gnecco, R. Bennewitz, T. Gyalog, C. Loppacher, M. Bammerlin, E. Meyer, H.-J. Güntherodt, Phys. Rev. Lett. **84**, 1172 (2000)
60. A. Socoliuc, R. Bennewitz, E. Gnecco, E. Meyer, Phys. Rev. Lett. **92**, 134301 (2004)

61. H. Brune, Surf. Sci. Rep. **31**, 121 (1998)
62. G.A. Tomlinson, Philos. Mag. S. 7 **7**, 905 (1929)
63. L. Prandtl, Z. Angew. Math. Mech. **8**, 85 (1928)
64. G.M. McClelland, in *Adhesion and Friction*, ed. by M. Grunze, H.J. Kreuzer (Springer, Heidelberg, Germany, 1989), pp. 1–16
65. Y. Sang, M. Dubé, M. Grant, Phys. Rev. Lett. **87**, 174301 (2001)
66. E. Riedo, E. Gnecco, R. Bennewitz, E. Meyer, H. Brune, Phys. Rev. Lett. **91**, 084502 (2003)
67. H. Hölscher, A. Schwarz, W. Allers, U.D. Schwarz, R. Wiesendanger, Phys. Rev. B **61**, 12678 (2000)
68. J. Kiely, J. Houston, Phys. Rev. B **57**, 12588 (1998)
69. G.L.W. Cross, A. Schirmeisen, P. Grütter, U.T. Dürig, Nat. Mater. **5**, 370 (2006)
70. N. Sasaki, M. Tsukada, Jpn. J. Appl. Phys. **39**, L1334 (2000)
71. L.N. Kantorovich, T. Trevethan, Phys. Rev. Lett. **93**, 236102 (2004)